Advanced Materials

ADVANCED MATERIALS
www.advmat.de

RESEARCH ARTICLE

Electrically Tunable and Linearly Polarized Mid-Infrared Photoluminescence in 2D Tellurium

Delang Liang[1,2] | Shiyu Wang[2] | Jingsi Qiao[3] | Chun Huang[3] | Zhi Zheng[4] | Yushuang Zhang[1] | Mingyang Qin[2] | Yuchun Chen[2] | Lin Li[4] | Jing Liu[5] | Wei Ji[6] | Shula Chen[1] | Changgan Zeng[4] | Anlian Pan[1,7] | Dong Sun[2,8,9,10]

[1]Key Laboratory for Micro-Nano Physics and Technology of Hunan Province, Hunan Institute of Optoelectronic Integration, College of Materials Science and Engineering, Hunan University, Changsha, P. R. China | [2]International Center for Quantum Materials, School of Physics, Peking University, Beijing, P. R. China | [3]School of Integrated Circuits and Electronics, School of Interdisciplinary Science and School of Physics, Beijing Institute of Technology, Beijing, P. R. China | [4]CAS Key Laboratory of Strongly Coupled Quantum Matter Physics, Department of Physics, University of Science and Technology of China, Hefei, P. R. China | [5]State Key Laboratory of Precision Measurement Technology and Instruments, School of Precision Instruments and Opto-electronics Engineering, Tianjin University, Tianjin, P. R. China | [6]Beijing Key Laboratory of Optoelectronic Functional Materials & Micro-Nano Devices, School of Physics, Renmin University of China, Beijing, P. R. China | [7]School of Physics and Electronics, Hunan Normal University, Changsha, P. R. China | [8]School of Physics, Zhengzhou University, Zhengzhou, P. R. China | [9]Collaborative Innovation Center of Quantum Matter, Beijing, P. R. China | [10]Frontiers Science Center For Nano-optoelectronics, School of Physics, Peking University, Beijing, P. R. China

Correspondence: Changgan Zeng (cgzeng@ustc.edu.cn) | Anlian Pan (anlian.pan@hnu.edu.cn) | Dong Sun (sundong@pku.edu.cn)

Received: 3 September 2025 | **Revised:** 16 November 2025 | **Accepted:** 12 December 2025

Keywords: electro-optical switches | linear polarization | mid-infrared photoluminescence | tellurium nanoflakes

ABSTRACT

The integration of electronic and photonic chips hinges on the availability of efficient light sources and modulators that are compatible with on-chip interconnects. Among these, mid-infrared (mid-IR) emitters are especially critical, as they enable low-loss transmission through atmospheric windows and unlock powerful capabilities for molecular fingerprinting and chemical sensing. In this study, we demonstrate that 2D tellurium (Te) nanoflakes can serve as highly efficient, electrically tunable, and linearly polarized mid-IR emitters. Leveraging the narrow direct bandgap (≈0.36 eV) and anisotropic crystal symmetry of Te nanoflakes, we achieve electrically tunable mid-IR photoluminescence (PL) with near-complete PL intensity modulation, a stable emission wavelength (≈3.4 µm), and near-perfect linear polarization. In addition, we demonstrate a dual-gate device that allows independent control of the electrostatic doping and vertical electric field, and further theoretical analysis reveals that the electrical tunability of the PL intensity originates primarily from the gate-controlled carrier density. Building on this robust control, we demonstrate high-speed electro-optical switches and programmable logic gates for on-chip encryption, underscoring the excellent compatibility of Te with advanced optoelectronic circuits. Collectively, these advances establish Te as a cornerstone material for hybrid electronic-photonic systems, directly addressing the urgent demand for mid-IR components in next-generation optical interconnects.

1 | Introduction

Electro-optical switches with large modulation depths are fundamental components of modern optoelectronic systems, and play vital roles in telecommunications, sensing, imaging and photonic computing [1, 2]. The emergence of low-dimensional materials especially 2D layered materials, has further transformed the field by enabling unprecedented device miniaturization and

---

[Correction added on January 7, 2026, after first online publication: Figure 1+4 has been replaced.]

seamless integration with on-chip photonic integrations [3, 4]. In particular, electrically controlled photoluminescence (PL) in 2D layered semiconductors has emerged as a promising approach for constructing compact, on-chip electro-optical switches. Extensive studies in 2D layered materials have demonstrated that electrostatic doping can tune the emission character from neutral excitons to trions [5] or suppress nonradiative recombination to enhance the PL [6, 7], and the external electric field enables the modulation of interlayer excitons or band structure engineering to tailor the PL emission [8, 9]. These studies have also explored coupling with plasmonic nanostructures to increase the modulation depth [10]. Despite their pivotal role in advancing next-generation photonic technologies, the development of compact, tunable light sources and modulators suitable for on-chip integration remains largely limited to the visible and near-infrared spectral ranges. This has left a significant technological gap in the mid-infrared range (mid-IR, ≈3–12 μm), which is essential for realizing diverse applications ranging from environmental monitoring to medical diagnostics and free-space communication [11–13].

Addressing this gap with conventional narrow-bandgap semiconductors (e.g., InAs, HgCdTe) is challenging owing to their high fabrication costs, complex epitaxial growth requirements, and poor on-chip integration compatibility. Among 2D materials, black phosphorus (BP) is a promising material option in this regard, but its unstable nature under ambient conditions and unintended bandgap shift under gate tuning severely limit its practical application [14]. Although alloying with arsenic to form black arsenic-phosphorus (b-$As_{1-x}P_x$) can modestly improve stability, the PL quantum yield decreases severely with increasing arsenic concentration owing to higher defect densities [15, 16].

Tellurium (Te), an elemental semiconductor with a narrow bandgap of ≈0.36 eV, has emerged as a compelling candidate for mid-IR optoelectronic devices. Early studies on bulk Te reported luminescence and lasing under electron-beam excitation (1965) and optical pumping (1979) [17, 18]. More recently, mid-IR PL from polycrystalline Te films has been observed, with quantitative measurements revealing an internal quantum yield of 2.0% at room temperature [19, 20]. These findings underscore Te's potential as a mid-IR emitter. Nevertheless, the electrical tunability of PL emission in Te, a critical attribute for developing tunable mid-IR emitters, remains unexplored. Additionally, as a highly anisotropic material, Te also shows great potential as a highly polarized emitter, which is ideal for polarization-sensitive optoelectronic applications.

Herein, we demonstrate an electrically tunable mid-IR PL with a large modulation depth of Te nanoflakes via integration into dual-gate field-effect devices. Our theoretical analysis reveals that PL modulation primarily arises from gate-tunable doping changes rather than the modulation of the electronic band structure, as previously observed in black phosphorus. Furthermore, a systematic investigation of polarization-dependent PL spectra revealed stable emission at ≈3.4 μm and nearly perfect linear polarization along the crystalline a-axis regardless of the gate-voltage configuration. More importantly, the dual-gate architecture enables complete PL quenching and programmable control of the PL output, allowing us to realize high-speed electro-optical switches and logic gate operations, which is ideal for mid-IR optoelectronic information processing. These results establish Te as a promising platform for next-generation multifunctional mid-IR optoelectronic devices with potential applications spanning optical communications, optical computing, and on-chip photonic integration.

2 | Results

2.1 | Device Fabrication and Basic Characterization

The Te nanoflakes used in our work were synthesized via a hydrothermal method and then transferred onto SiO_2 (285 nm)/Si substrates through a drop-casting process (see Methods for synthesis details). As shown in Figure 1a, the crystal structure of Te consists of 1D helical atomic chains aligned parallel to each other and interconnected by van der Waals forces, extending along the crystallographic c-axis [21]. The orientation of the c-axis in the Te nanoflake was identified from the long edge in the optical image and further confirmed by polarization-dependent Raman spectroscopy as shown in Figure S1.

To investigate the electrically tunable PL of Te nanoflakes, a dual-gate field-effect transistor (FET) device was fabricated on the basis of a graphite/hexagonal boron nitride/tellurium (Gr/h-BN/Te) heterostructure, as schematically illustrated in Figure 1b. This device architecture not only allows for electrically tunable optical measurements via independent control of the top and bottom gates, but also enables independent modulation of the carrier density (doping level) and vertical electric field by applying appropriate top and bottom gate configurations [22, 23]. Few-layer graphite is selected as the top-gate electrode material, which offers excellent transparency in the mid-IR region and thereby facilitates accurate PL measurements. The optical image of the device is presented in the inset of Figure 1c, where the Gr/h-BN heterostructure was assembled using a polymer-free dry transfer method and placed atop the Te flake on the SiO_2/Si substrate (see Figure S2) [24]. The thicknesses of the h-BN and Te nanoflakes were measured to be 8.4 and 44.6 nm, respectively, as confirmed by atomic force microscopy (AFM) (Figure S3).

The output characteristics of the FET exhibit linear behavior at 25 K (Figure S4), indicating good ohmic contacts between the electrodes and the Te channel. The transfer characteristics were measured by independently tuning the top and bottom gates with a drain-source bias of V_{DS} = 0.1 V. The results are shown by the red and blue curves in Figure 1c, respectively. As the gate voltage increases, the channel current gradually decreases, indicating typical p-type semiconducting behavior, which is consistent with previous reports [25]. Notably, the current is fully suppressed at positive gate voltages, suggesting a transition in the hole concentration—from accumulation to depletion—as the gate voltage shifts from negative to positive. This transition occurs without reaching the inversion regime within the applied voltage range.

Figure 1d presents a schematic illustration of the PL process, which uses a 1064 nm continuous-wave (CW) laser as the excitation source, along with the corresponding band structure

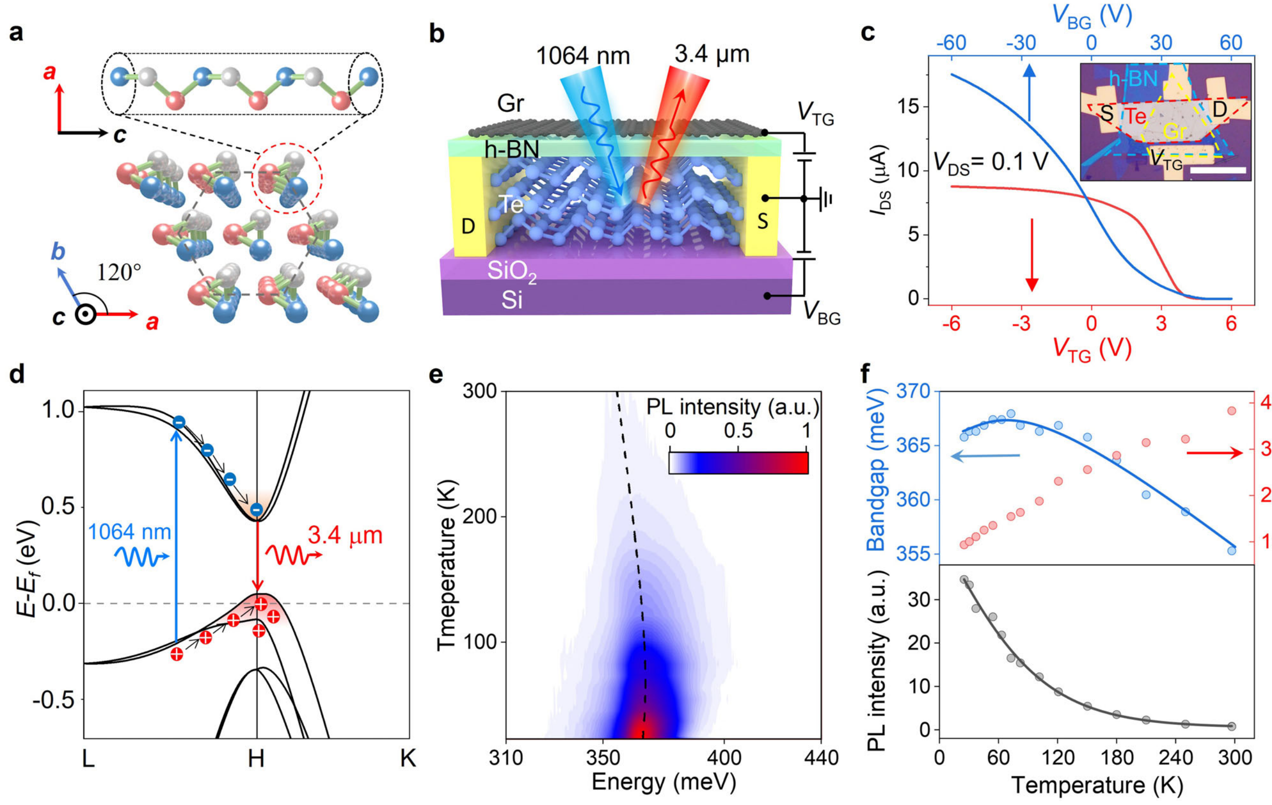

FIGURE 1 | Crystal structure and PL characterization of Te nanoflakes. a) Crystal structure of Te nanoflakes. b) Schematic illustration of the dual-gate device with few-layer graphite and Si serving as the top and bottom gates for electrical characterization and tunable PL measurements, respectively. c) Source-drain current (I_{DS}) measurement of the transistor as a function of the top gate (red line) and bottom gate (blue line), where $V_{DS} = 0.1$ V. The inset shows the optical micrograph of the dual-gate device (Te nanoflake, few-layer graphite and h-BN, corresponding to the red, yellow and blue dashed line regions, respectively). Scale bar: 30 μm. d) Schematic illustration of the PL emission process under 1064-nm excitation and the band structure of Te. e) Contour map of the PL spectra as a function of temperature, which varied from 25 to 300 K. The black dashed line represents the peak position. f) Extracted FWHM, peak position and integrated intensity of the PL spectrum as a function of temperature. The blue solid lines represent the fitting of the temperature-dependent bandgap via the modified Manoogian–Leclerc model, and the gray solid line is a guide to the eye.

of Te nanoflakes, which possess a bandgap of approximately 0.365 eV [26]. Temperature-dependent PL spectra were recorded over a range from 25 to 300 K, as shown in Figure 1e. The PL peak position, highlighted by the black dashed line in Figure 1e, closely matches the bandgap energy of the Te nanoflakes. As depicted in Figure 1f, the PL spectra reveal a broad emission peak, with the full width at half maximum (FWHM) varying between 21 and 38 meV. The excellent agreement between the PL energy and the bandgap, combined with the relatively large FWHM, suggests that the observed radiative recombination originates from free carriers rather than excitons owing to the negligible exciton binding energy in Te nanoflakes [27]. Notably, the bandgap exhibits a nonmonotonic temperature dependence: it increases slightly from 0.366 eV at 25 K to 0.368 eV at 75 K and then decreases to 0.355 eV at 300 K, as shown in Figure 1f. This nonmonotonic bandgap behavior is consistent with previously reported temperature-dependent shifts in the absorption edge, which result from the competing effects of thermal expansion and electron–phonon interactions [28]. Meanwhile, the PL intensity decreases with increasing temperature, which can be attributed to the thermal activation of nonradiative recombination centers and recombination via trap states within the forbidden gap (Shockley–Read–Hall theory) [29, 30]. Unless otherwise specified, all subsequent measurements were performed at 25 K.

To validate the outstanding PL of the Te nanoflakes, we compared their emission directly with that of as-exfoliated BP. Under the same experimental conditions, the PL intensity of a Te nanoflake (≈70 nm) is more than two orders of magnitude greater than that of a BP nanoflake (≈30 nm), as shown in Figure S5. Furthermore, to quantitatively evaluate the luminescence efficiency, we measured the photoluminescence quantum yield (PLQY) of Te nanoflakes (details in the Experimental Section). At 25 K, the internal PLQY reaches 16.8% for the brightest Te nanoflake (Figure S6), significantly surpassing the reported 2% for polycrystalline Te films at room temperature [20]. This remarkable PLQY highlights the advantages of single-crystal Te nanoflakes, which firmly establish 2D Te as an efficient and bright mid-IR emitter.

2.2 | Electrically Tunable PL Emission

To investigate the electrically tunable characteristics, we measured the PL spectra as a function of the top gate (V_{TG}, ranging from −6 to 6 V, with $V_{BG} = 0$ V) and bottom gate (V_{BG}, ranging from −60 to 60 V, with $V_{TG} = 0$ V) using an excitation power of 170 μW, as shown in Figure 2a. The PL intensity decreases significantly as either V_{TG} or V_{BG} is swept from negative to positive values.

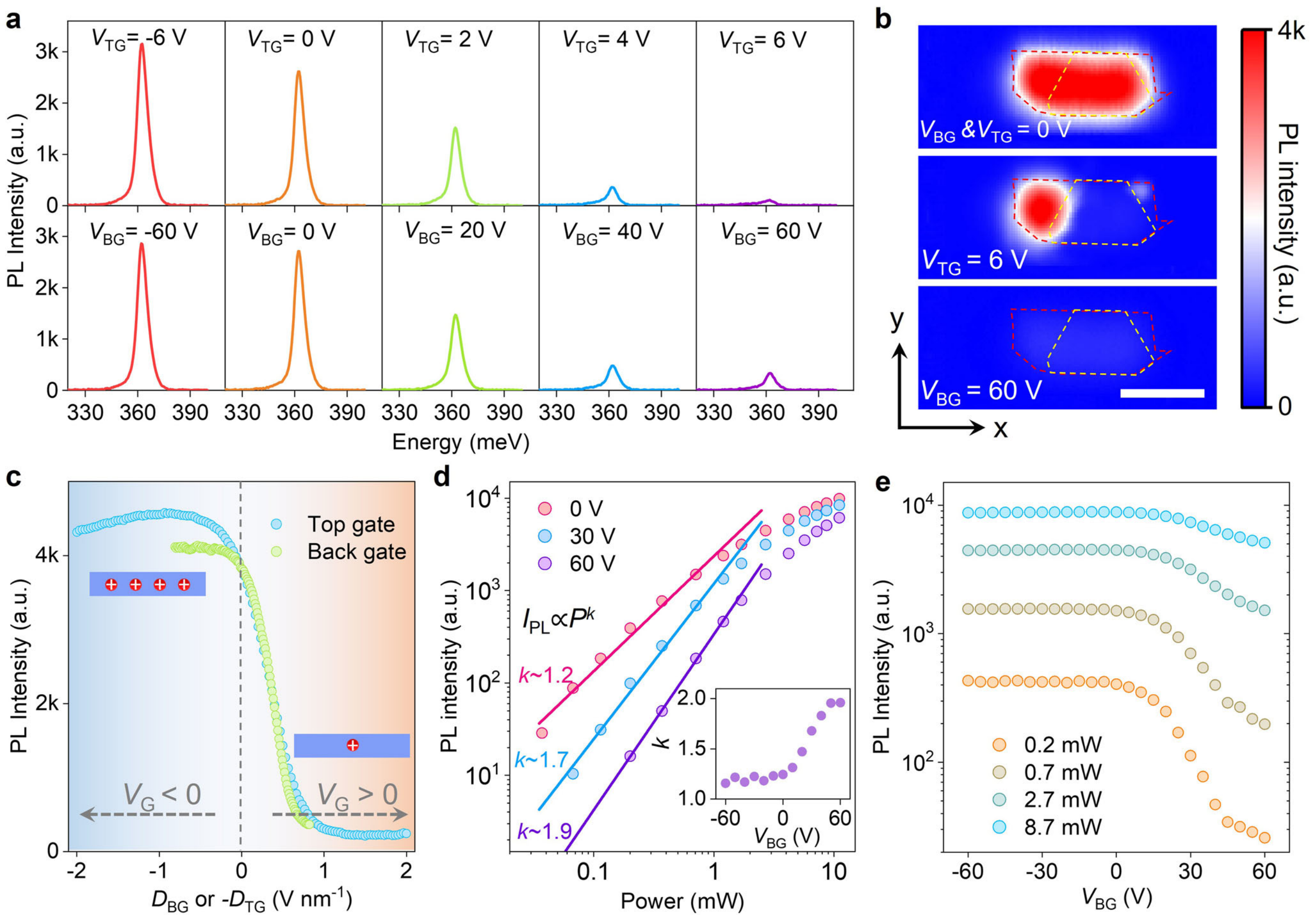

FIGURE 2 | Electrically tunable PL spectra. a) PL spectra of the dual-gate device measured at different top-gate (V_{TG}) and bottom-gate (V_{BG}) voltages. b) Spatial maps of the integrated PL intensity from the dual-gate device at zero gate voltage, V_{TG} = 6 V, and V_{BG} = 60 V. The red dashed line outlines the Te nanoflake, excluding the metal contacts, and the yellow dashed line indicates the heterostructure region (Gr/h-BN/Te). These measurements were performed with a step size of 1 µm. Scale bar: 30 µm. c) Integrated PL intensity as a function of the electric displacement field. The right and left blue boxes illustrate the hole density in the Te nanoflake under positive and negative $V_{G,}$ respectively, where V_G represents either V_{TG} or V_{BG}. d) Power-dependent PL intensity under different bottom-gate voltages. The solid lines indicate fits for $p < 1.2$ mW, with the exponents marked nearby. The inset shows the fitted exponent k as a function of the bottom-gate voltage. e) PL intensity as a function of the bottom-gate voltage under different excitation powers.

This effect is directly illustrated in Figure 2b, which presents PL mapping images under three representative conditions: zero gate voltage, $V_{TG} = 6$ V, and $V_{BG} = 60$ V. The PL intensities are greatly suppressed when positive gate voltages are applied to either gate. The local top gate, constructed from few-layer graphite (yellow dashed outline in Figure 2b), enables selective control of the PL intensity distribution; for $V_{TG} = 6$ V, PL suppression is confined to the region covered by the graphite top gate, while other areas of the Te nanoflake remain unaffected. In contrast, the global bottom gate enables uniform tuning of the PL emission across the entire Te nanoflake. Meanwhile, the PL intensity from the covered region is >95% of that from the bare Te region, indicating that Gr/h-BN does not significantly degrade the external PL efficiency of the device.

Figure 2c shows the integrated PL intensities as functions of the top and bottom electrical displacement fields (D_{BG} or $-D_{TG}$), where $D_{BG} = \varepsilon_{SiO_2} V_{BG}/d_{SiO_2}$ and $D_{TG} = -\varepsilon_{hBN} V_{TG}/d_{hBN}$, respectively. Here, $\varepsilon_{SiO_2} = 3.9$ and $\varepsilon_{hBN} = 3.5$ represent the relative permittivity, and d_{SiO_2} and d_{hBN} represent the thicknesses of the h-BN and SiO$_2$ layers, respectively [31]. In such a measurement, the integrated PL intensity is collected without a monochromator, which integrates the emission photons over all wavelengths. The PL intensity slightly increases when negative gate voltages are applied and decreases significantly when positive gate voltages are applied. For equivalent displacement fields, similar PL intensities are observed via either gate, although the maximum modulation effect is more prominent when the top gate is tuned. To further quantify the gating effect, we define the modulation depth as $M = I_{PL}/I_0$, where I_{PL} and I_0 denote the modulated and initial PL intensities, respectively. The maximum and minimum values of M are 108% and 10%, respectively, for bottom-gate tuning, and a greater range of 120% and 6%, respectively, for top-gate tuning. Repeatability tests conducted on six dual-gate devices demonstrate consistent PL tunability and modulation depths (Figure S7 and Table S1). Minor variations observed among these devices are attributed to differences in Te nanoflake thickness, doping levels, and h-BN thickness.

2.3 | Radiative Recombination Model

For radiative recombination involving free carriers, the background carrier density is particularly important [32]. Before photoexcitation, the net carrier density within Te nanoflakes can be estimated using the parallel-plate capacitor model for a 2D FET device, and expressed as [6, 33]:

$$n - p = C_{\mathrm{OX}}\left(V_{\mathrm{G}} - V_{\mathrm{th}}\right)/q \tag{1}$$

where n and p represent the background electron and hole concentrations (including both natural and electrostatic doping), respectively, while V_{G}, V_{th}, C_{OX} and q correspond to the gate voltage, threshold voltage, gate oxide capacitance, and elementary charge, respectively. The PL intensity (I_{PL}) is directly proportional to the net radiative recombination rate R, given by $R = B(n + \Delta n)(p + \Delta p)$, where $\Delta n = \Delta p$ represents the photogenerated carrier concentration and B is the radiative recombination coefficient [34]. Given the inherently high hole density ($\approx 10^{18}$ cm^{-3}) in Te nanoflakes at 25 K, the electron density n may be neglected, simplifying the relationship to:

$$I_{\mathrm{PL}} \propto B\Delta n\left(p + \Delta n\right) \tag{2}$$

Accordingly, modulation of the carrier density via the gate voltage directly impacts the radiative recombination rate—and thus the PL intensity. Experimentally, a slight increase in the PL intensity is observed under negative gate voltages. This is attributed to screening effects at the Te/dielectric interface, which limit further increases in the hole concentration [35]. Conversely, applying positive gate voltages depletes holes, resulting in pronounced PL quenching. The top-gate configuration achieves a greater modulation depth, likely because the upper layer, where PL emission mainly originates, is more effectively controlled by the top gate.

To further elucidate these effects experimentally, power-dependent PL measurements were performed under different bottom-gate voltages (Figure 2d). At low excitation power (P < 1.2 mW), the PL intensity exhibits a superlinear power dependence, following $I_{\mathrm{PL}} \propto P^k$, with the exponent k increasing from 1.2 to 1.9 as V_{BG} varies from −60 to 60 V (see the inset in Figure 2d). At higher excitation powers (P > 1.2 mW), the PL intensity deviates from this trend because of laser-induced heating and dominant Auger recombination at high carrier densities. Figure 2e depicts the gate-dependent PL intensity under different excitation powers. Notably, although the modulation depth of the PL intensity gradually decreases as the excitation power increases, the absolute intensity difference becomes more pronounced.

This observed power-law behavior is consistent with the recombination model described above. At low excitation powers (P < 1.2 mW), the photogenerated carrier concentration Δn is proportional to P. Under negative gate voltages, where $p \gg \Delta n$, the PL intensity increases linearly with power ($I_{\mathrm{PL}} \propto P$). In contrast, under sufficiently positive gate voltages, the hole density is significantly depleted ($p \ll \Delta n$), and the PL intensity exhibits a quadratic dependence ($I \propto P^2$). Thus, as the gate voltage approaches depletion conditions, the exponent k transitions from approximately 1 (high hole density) to nearly 2 (low hole density). At high excitation powers, where $\Delta n \gg p$ and photogenerated carriers dominate, the influence of background carriers diminishes, accounting for the observed reduction in the PL modulation depth. The simulation results of the power- and gate-dependent PL intensities based on a more detailed recombination model are in good agreement with the experimental data, as shown in Figure S8.

2.4 | Dual-Gate Modulation PL Emission

To distinguish the individual contributions of the vertical electric field and electrostatic doping to PL modulation, Figure 3a displays a map of the integrated PL intensity for the dual-gate device as functions of D_{TG} and D_{BG}. The intensity was normalized to the value at zero gate voltage, and the raw data are presented in Figure S9. An enhanced PL is observed in the negative gate regions (V_{TG} and $V_{\mathrm{BG}} < 0$ V), corresponding to a high hole density. In contrast, almost completely suppressed PL ($M \approx 0.4\%$) appears in the positive gate region, as indicated by the white dashed area in Figure 3a, which corresponds to a low carrier density with a simultaneously applied vertical electric field.

In this dual-gate device, electrostatic doping is governed by $\Delta D = D_{\mathrm{BG}} - D_{\mathrm{TG}}$, while the average vertical displacement field can be expressed as $D_{\mathrm{av}} = (D_{\mathrm{TG}} + D_{\mathrm{BG}})/2$. By independently setting ΔD or D_{av} to zero, the effects of the vertical electric field (D_{av}, $\Delta D = 0$ V nm^{-1}) and electrostatic doping (ΔD, $D_{\mathrm{av}} = 0$ V nm^{-1}) on PL modulation can be isolated. Figure 3b presents the PL intensity as a function of the vertical electric field (D_{av}, $\Delta D = 0$ V nm^{-1}) and electrostatic doping (ΔD, $D_{\mathrm{av}} = 0$ V nm^{-1}), corresponding to the red and gray dashed lines in Figure 3a, respectively. For electrostatic doping, we observe M values as high as 132% at $\Delta D = -1.6$ V nm^{-1} and 4% at $\Delta D = 1.6$ V nm^{-1}, exceeding those achieved via single-gate modulation. In contrast, when a vertical electric field is applied, the PL intensity decreases with increasing displacement field, regardless of the polarity of the displacement field. This PL suppression under a vertical electric field is attributed to electric-field-induced band bending, as schematically illustrated in Figure 3c. This band bending leads to spatial separation of electrons and holes, reducing their wavefunction overlap and, consequently, the probability of radiative recombination [14, 36]. These results demonstrate that both electrostatic doping and the vertical electric field can effectively modulate the PL intensity, with electrostatic doping generally producing a larger modulation depth, whereas the vertical electric field consistently suppresses the PL regardless of the field polarity.

Further spectral analysis (Figure 3d) revealed that under displacement fields up to 0.8 V nm^{-1}, the bandgap essentially remains unchanged (0.363–0.364 eV, <16 nm shift in emission wavelength at 3.4 µm), indicating near invariance of the bandgap during modulation. This behavior stands in stark contrast to that of BP, a representative mid-infrared emitter, in which a vertical electric field induces a pronounced bandgap reduction owing to the giant Stark effect [14, 35, 37]. To further elucidate the very weak field dependence of the bandgap, density functional theory (DFT) calculations based on a tight-binding model were performed. As shown in Figure 3e, under vertical electric fields as

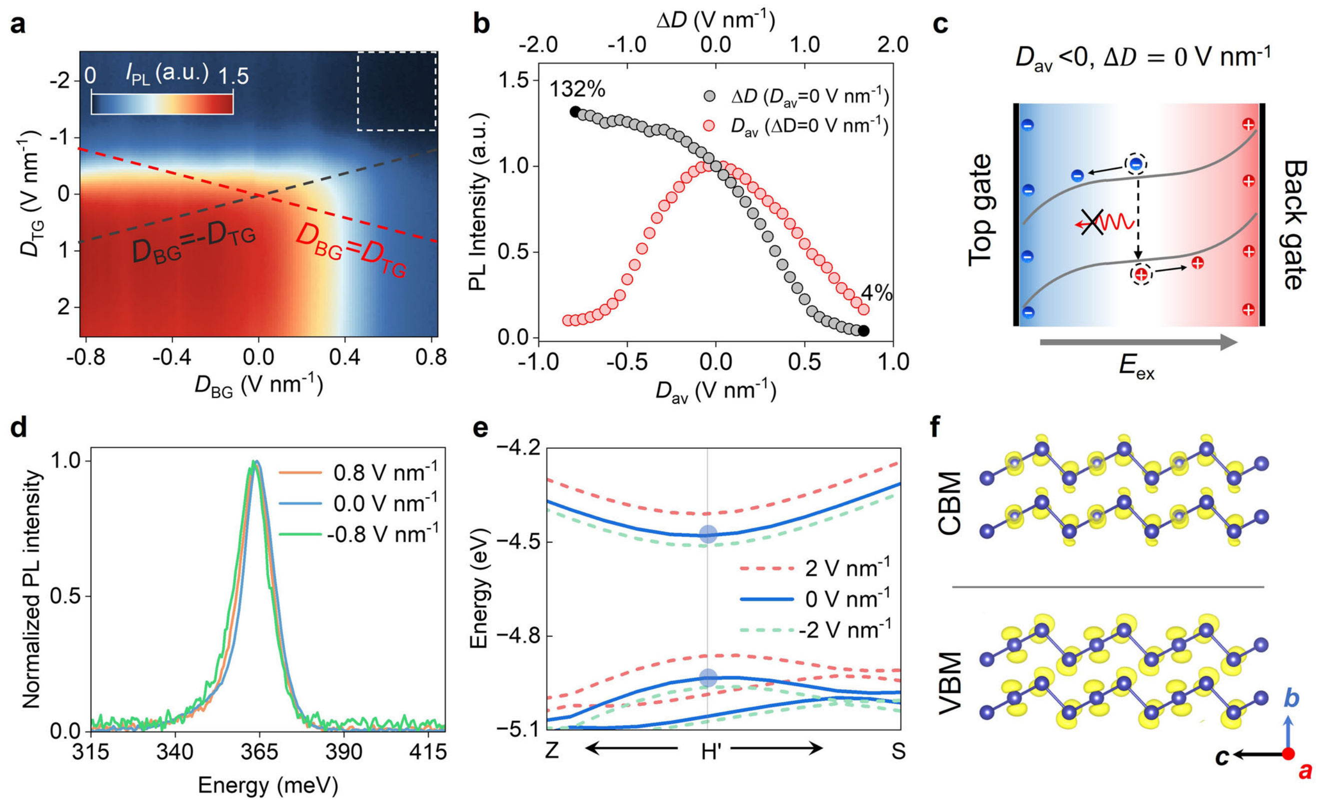

FIGURE 3 | Vertical electric field-induced tunable PL. a) Color plot of the integrated PL intensities as a function of D_{TG} and D_{BG}. The gray (red) dashed line corresponds to a constant carrier density (displacement) profile. b) Extracted PL intensity as a function of D_{av} and ΔD from the gray and red dashed lines in panel a. c) Schematic of energy band diagrams under a vertical electric field ($D_{av} < 0,\ \Delta D = 0$ V nm^{-1}). The arrow labeled E_{ex} marks the direction of the external electric field. d) Normalized PL spectra under different D_{av} with $\Delta D = 0$ V nm^{-1}, showing a small bandgap shift of less than 1 meV. e) Band structures of the Te nanoflake near the H' point (located between Z–S) under a ± 2 V nm^{-1} electric field in comparison with no external electric field. For simplicity, only the lowest conduction band and the two highest valence bands are plotted. f) Real space distributions of the band-decomposed partial charge density for the CBM and VBM around the H' point, using an isosurface of 0.01 e bohr^{-3}. The charge density is highly localized around Te atoms for both the CBM and VBM.

large as 2 V nm^{-1}, the band structure only slightly shifts, with the bandgap changing by less than 0.01 eV. Furthermore, calculations of the squared transition dipole moments (Figure S10) confirm that the transition probability near the band edge remains nearly constant under applied electric fields. This negligible effect of the electric field on both the bandgap and transition can be attributed to the highly localized wavefunctions of Te around the valence band maximum (VBM) and conduction band minimum (CBM), as further illustrated in Figure 3f. These localized states result in a concentrated electron distribution, which significantly reduces the influence of the electric field on both the bandgap and the transition dipole moment. Additionally, the Raman spectra (Figure S11) remain unchanged under varying gate voltages, ruling out field-induced lattice structural changes [38]. Taken together, these results demonstrate that dual-gate modulation enables robust and nearly bandgap-invariant control of the PL in 2D Te nanoflakes, providing unique advantages for mid-infrared optoelectronic applications.

2.5 | Linearly Polarized PL Emission

To examine the polarization dependence of both the excitation light and the PL emission, polarization-dependent PL measurements were performed. These measurements were carried out in two configurations (Figure S12). In the first configuration, the polarization of the incident laser (P_{in}) is rotated and aligned along either the a- or c-axis, while the PL spectra are collected without an analyzer before the detector. The PL spectrum under excitation polarized along the c-axis is lower than that along the a-axis (Figure 4a), which can be attributed to anisotropic optical absorption at 1064 nm. In the second configuration, the excitation laser polarization was still aligned along the a- or c-axes, while the polarization of the PL was measured at different detection polarization angles θ (0° corresponding to the c-axis). Figure 4b shows that the integrated PL intensity reaches a maximum when the detection polarization angle $\theta = 90°$ and is minimal at $\theta = 0°$, regardless of the excitation polarization along the a- or c-axis. The degree of linear polarization (DOLP), defined as DOLP = $(I_{max}-I_{min})/(I_{max}+I_{min})$, exceeds 98%, indicating that the PL emission is highly linearly polarized along the a-axis.

This remarkable observation of strongly polarized PL emission is consistent with previous PL experimental results in bulk Te, as well as first-principles simulations of Te crystals, which indicate that optical interband transitions between the VBM and CBM are forbidden for emission along the c-axis (E//c) [17, 39]. Furthermore, polarization-dependent PL measurements

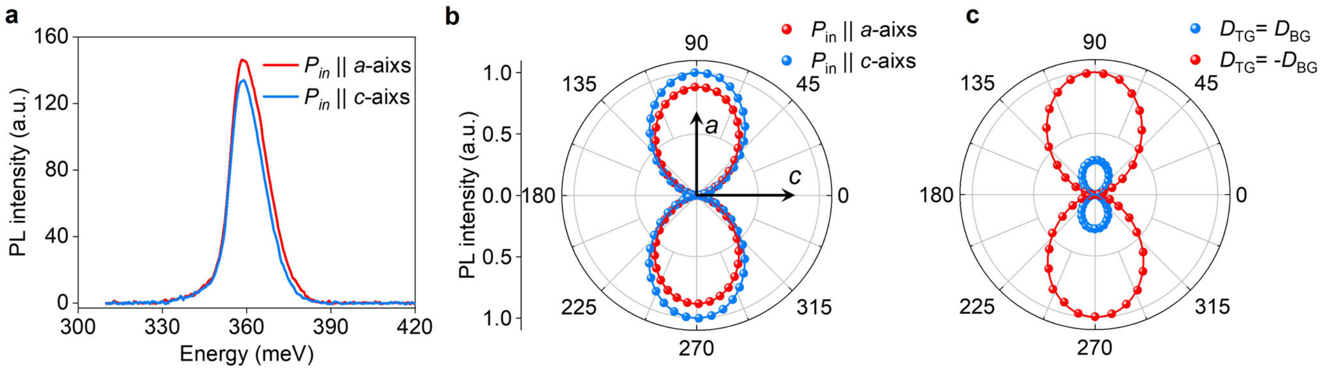

FIGURE 4 | Linearly polarized PL of Te nanoflakes under 1064 nm excitation. a) PL spectra of the Te nanoflake under excitation polarization parallel to the *a*- and *c*-axes. b) Integrated PL intensity as a function of the detection polarization angle θ, with blue and red data points representing incident light polarization parallel to the *a*- and *c*-axes, respectively. The crystal orientations are labeled with black arrows. c) Polarization analysis of the PL emission under a vertical electric field (blue points) or electrostatic doping (red points) with $D_{TG} = 0.5$ V nm^{-1}. All angular dependences show a nearly perfect $\cos^2\theta$ pattern (solid curves).

under different gate voltages (Figure 4c) show that, regardless of the gate voltage configuration, the PL emission from the Te nanoflake retains its nearly perfect linear polarization (DOLP > 98%). These results demonstrate that the symmetry-forbidden transitions along the *c*-axis persist under an external electric field and different doping levels.

2.6 | Demonstration of High-Speed Electro-Optic Logic Gates

The ability to electrically tune the PL enables the development of multifunctional mid-IR nonlinear optoelectronic devices. As a proof of concept, we utilized dual-gate modulator cells to demonstrate electro-optic logic gates for signal processing, as illustrated in Figure 5a. Practical electro-optic switches and logic gates demand both high operational stability and fast response speeds. The negligible hysteresis observed during bidirectional gate-voltage sweeps (Figure S13) and the device functionality maintained for over one year (Figure S14) demonstrate the excellent reversibility and stability of the dual-gate device. To evaluate the dynamic PL performance of the dual-gate device, we applied a square-wave top-gate voltage of ±6 V at a frequency of 10 kHz and monitored the PL intensity variation using an oscilloscope, as shown in Figure 5b. The PL intensity displays stable switching between the on and off states. Moreover, a zoom-in of the time window from -5 to 5 µs and 45 to 55 µs clearly indicates a switching time of 1.5 µs. This switching time is limited by the response time of the InSb detector used in the measurement, and the intrinsic device performance should be faster. A comprehensive comparison of the performance metrics with other PL-based electro-optic modulators is provided in Table S2.

Building on these results, we demonstrated an optical information encryption scheme leveraging the dual-gate modulator. Specifically, the excitation light (on/off) serves as the first optical input (In1), and the gate voltage polarity (positive/negative) acts as the second input (In2), as shown in Figure 5c. This configuration allows the implementation of a logic AND gate, in which the mid-IR PL emission serves as the programmable output signal, controlled by the excitation light and gate voltage. In addition, Boolean NOR gates—commonly employed as core elements in decision and comparison circuits for various applications such as data encryption—can be realized by assigning the top gate and bottom gates as In1 and In2, respectively, with constant light excitation power. Figure 5d shows the truth table and flow chart for the proposed NOR logic gates. For example, the input electrical signal 'Te' (In1) was encoded via the American Standard Code for Information Interchange (ASCII) and, together with a key (In2), input into the NOR gate, yielding an encrypted mid-IR optical signal output, as shown in Figure 5e.

3 | Conclusion

In summary, we have demonstrated deep electrical modulation of the mid-IR PL intensity in 2D Te-based dual-gate devices, addressing the critical need for efficient mid-IR light sources and modulators. Notably, two key intrinsic properties were preserved under electrical control: a stable emission wavelength and near-perfect linear polarization. The remarkable wavelength stability is attributed to a negligible Stark effect, as confirmed by theoretical calculations. By decoupling the vertical electric field and electrostatic doping effects, our analysis reveals that the PL intensity modulation is governed primarily by the gate-controlled carrier density. Building on these properties, we have successfully implemented high-speed electro-optical switches and logic gates, demonstrating a clear pathway toward on-chip optical encryption. Our work not only introduces a novel class of mid-IR electro-optical modulators but also provides a comprehensive understanding of the tunable optical properties of Te under gate control. Looking forward, the performance of Te-based devices may be further optimized by (i) enhancing the quantum yield through targeted chemical functionalization [40], (ii) coupling with plasmonic lattices, circular Bragg gratings or hyperbolic metamaterials [10, 41, 42], and (iii) developing low-threshold lasing with appropriate cavity designs [43, 44]. On a broader scale, developing efficient light-emitting diodes based on p–n junctions, alongside progress in wafer-scale fabrication and on-chip integration with silicon photonics, will be crucial [3, 45–47]. These advancements could establish Te as a lead-

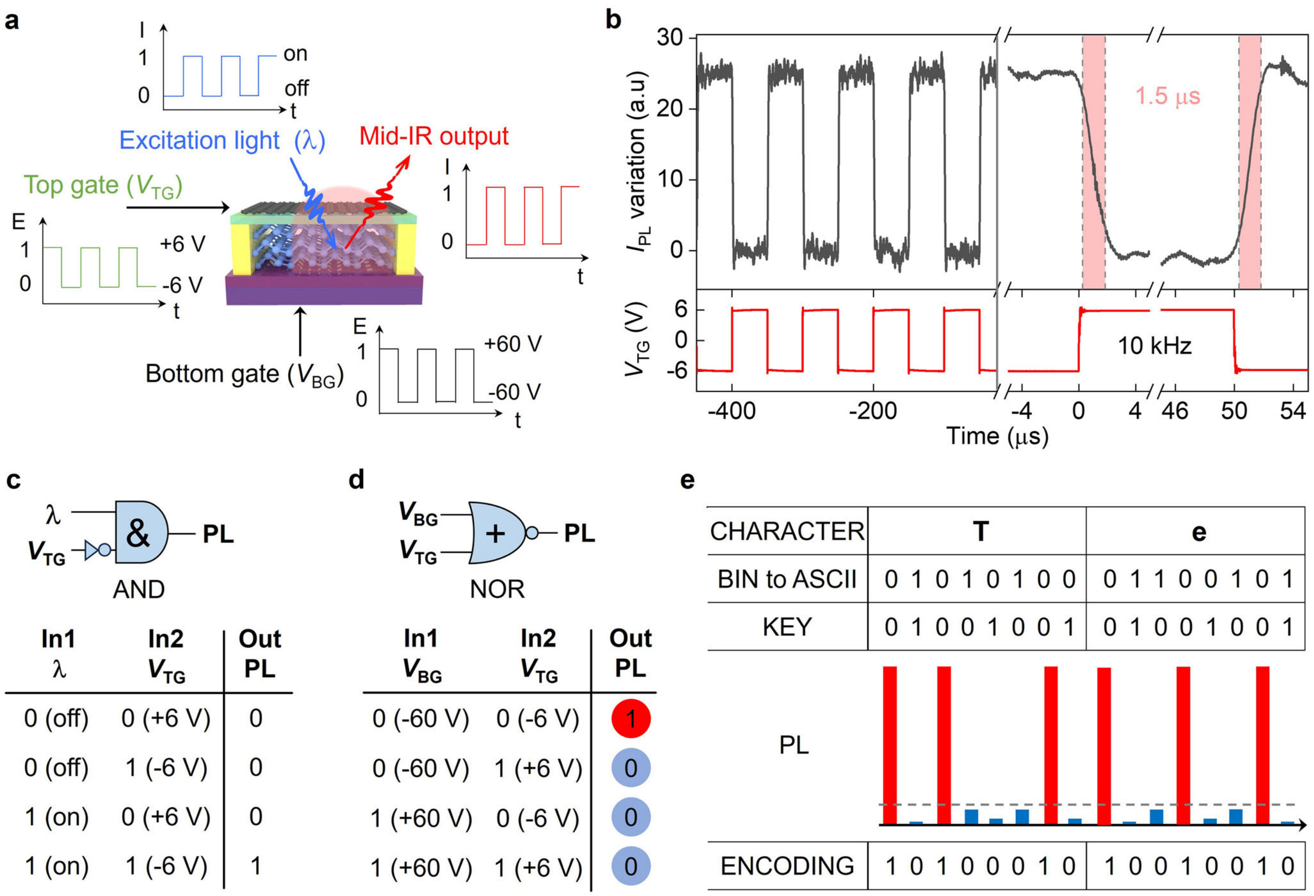

In1 λ	In2 V_{TG}	Out PL
0 (off)	0 (+6 V)	0
0 (off)	1 (-6 V)	0
1 (on)	0 (+6 V)	0
1 (on)	1 (-6 V)	1

In1 V_{BG}	In2 V_{TG}	Out PL
0 (-60 V)	0 (-6 V)	1
0 (-60 V)	1 (+6 V)	0
1 (+60 V)	0 (-6 V)	0
1 (+60 V)	1 (+6 V)	0

CHARACTER	T	e
BIN to ASCII	0 1 0 1 0 1 0 0	0 1 1 0 0 1 0 1
KEY	0 1 0 0 1 0 0 1	0 1 0 0 1 0 0 1
PL		
ENCODING	1 0 1 0 0 0 1 0	1 0 0 1 0 0 1 0

FIGURE 5 | Demonstration of high-speed electro-optic logic gates. a) Schematic illustration of the operating principle for the logic gate based on the dual-gate device. The mid-IR optical output signal is programmed by the excitation light and gate voltages. b) Time-resolved PL emission from the Te nanoflake (top panel) measured under a square-wave top gate voltage of ±6 V at 10 kHz (bottom panel), with constant light excitation power at 1064 nm. The right portion of the plot presents an enlarged view of the selected time window, highlighting a switching time of less than 1.5 μs (indicated by the shaded area), which is limited by the instrumentation response. c,d) Logic diagrams and truth tables for the logic AND and NOR gates under different input configurations, illustrating both the optical and electrical programming capabilities. e) Demonstration of mid-IR optical signal encryption based on the dual-gate configuration: the ASCII-encoded input ("Te") and a key are combined through the NOR logic operation, yielding a corresponding encrypted PL output waveform.

ing material platform for next-generation mid-IR optoelectronic technologies, such as mid-IR free-space communications and high-sensitivity spectroscopy, which can be widely used for molecular sensing, environmental monitoring, and medical diagnostics.

4 | Experimental Section

4.1 | Sample Preparation and Device Fabrication

Te nanoflakes were grown through a hydrothermal method [25, 48]. First, 3 g of polyvinylpyrrolidone (PVP, molecular weight = 58000) was dissolved in 32 mL of deionized (DI) water. Subsequently, 92 mg of Na_2TeO_3 was put into the PVP solution with continuous stirring. After that, 3.32 mL of ammonium hydroxide solution (25–28%, wt/wt%) and 1.68 mL of hydrazine hydrate (80%, wt/wt%) were added into the solution. Following 5 min of magnetic stirring, the solution was transferred into a 50 mL Teflon-lined stainless-steel autoclave and maintained at 180°C for 10 h. The resulting product was washed with deionized water to remove any residual ions. To fabricate the device, Te flakes were redispersed in ethyl alcohol and subsequently transferred onto a 285 nm SiO_2/Si substrate via drop-casting. The Gr/h-BN/Te heterostructure used for the dual-gate device was assembled via a polymer-free dry transfer method, and the fabrication details are presented in Figure S2. Electron beam lithography was then utilized to define electrode patterns. Ti/Pd/Au metal layers (0.5/20/70 nm) were deposited as electrode contacts via e-beam evaporation. The BP flakes (from HQ Graphene) were exfoliated and then transferred onto a 285-nm SiO_2/Si substrate inside an argon-filled glove box.

4.2 | PL Measurement

PL measurements were conducted using a self-built micro-PL measurement system. A steady 1064 nm CW laser was employed to excite the Te nanoflake. A ×40 reflective objective with a numerical aperture of 0.5 was used to focus the excitation laser onto the sample and collect the PL signal. All measurements were performed under vacuum in a liquid-helium-flow cryostat, enabling temperature control from 25–300 K. The cryostat was mounted on an XY scanner stage for spatial scanning. The collected PL signal was delivered to a spectrometer (Princeton SP2500i) equipped with a 150 g mm^{-1} grating and detected by a liquid nitrogen-cooled single-channel InSb photodetector with a preamplifier. The detector output was processed with a lock-in amplifier referenced to an optical chopper that modulated the excitation laser at 521 Hz. For gate-tunable PL measurements, gate voltages were applied using Keithley 2400 and 2612B source meters.

4.3 | PLQY Measurements

The PLQY of the Te nanoflakes was determined using the same experimental setup employed for the PL measurements. The PLQY is defined as the ratio of the number of emitted photons (N_{em}) to the number of absorbed photons (N_{abs}) [49]. The N_{abs} was calculated via the expression: $N_{\text{abs}} = \frac{P_{\text{ex}} \times A(1064\ \text{nm})}{E_{\text{ex}}}$, where P_{ex} represents the incident laser power illuminating to the material, $A(1064\ \text{nm})$ is the absorbance of the Te flake at 1064 nm, and E_{ex} represents the energy of a single excitation photon.

To quantify N_{em}, the collection efficiency of the setup was calibrated via a diffuse reflector (Thorlabs DG10-600-P01) as a Lambertian reflectance standard and a quantum cascade laser (QCL) emitting at 4.05 µm, a wavelength close to the Te PL emission peak [50]. The output power of the QCL (P_{ref}) was first measured via a high-sensitivity thermal power sensor positioned at the focal plane of the reflective objective. The signal intensity of the QCL (IR_{ref}) light reflected by the Lambertian standard was subsequently recorded via an InSb detector coupled to a spectrometer under the same PL measurement conditions. The ratio of the QCL output power (from the power sensor) to the signal intensity (from the InSb detector) was used to convert the measured PL intensity (IR_{PL}) of the Te flake into an emitted optical power. Corrections were applied to account for the wavelength-dependent optical system efficiency and detector responsivity at the reference wavelength ($\lambda_{\text{ref}} = 4.05$ µm) and the Te emission wavelength (λ_{PL}). The final expression for the PLQY is given by:

$$\text{PLQY} = \frac{P_{\text{ref}} \cdot E_{\text{ex}}}{P_{ex} \cdot A\,(1064\ \text{nm}) \cdot E_{\text{PL}}} \times \frac{IR_{\text{PL}}}{IR_{\text{ref}}} \times \frac{\eta_{\text{opt}}\,(\lambda_{\text{ref}})}{\eta_{\text{opt}}\,(\lambda_{\text{PL}})} \times \frac{D\,(\lambda_{\text{ref}})}{D\,(\lambda_{\text{PL}})} \tag{3}$$

where E_{PL} is the energy of a single emitted photon; IR_{PL} and IR_{ref} are the measured signal intensities of the Te PL and reference QCL light, respectively; η_{opt} is the optical system efficiency (including the reflective objective, mirrors, beam splitter, lenses, and monochromator); and $D(\lambda)$ is the detector responsivity at the respective wavelengths.

4.4 | DFT Calculations

First-principles calculations based on density functional theory (DFT) were conducted utilizing the generalized gradient approximation (GGA) for the exchange-correlation functional, in conjunction with a plane-wave basis set and the projector augmented wave (PAW) pseudopotentials [51], as implemented in the Vienna ab initio simulation package (VASP) [52]. van der Waals interactions were considered at the DFT-DF level with the optB88-vdW function [53]. The kinetic energy cutoff for the plane-wave basis set was set to 700 eV for all calculations. A k-mesh of 15×15×11 was used for both structural relaxation and electronic structure calculations of the primitive Te structure. For the layered Te system (6-layer structure, 6 L), a k-mesh of 1×15×11 was adopted. To simulate the effect of an external electric field, the 6 L layered structure was calculated, similar to the bulk system, as the introduction of a vacuum layer is required when an electric field is applied. All atoms in the cells were fully relaxed until the residual force on each atom was less than 5×10^{-3} eV Å^{-1}, and the total energy convergence criterion was set to 1×10^{-5} eV.

Author Contributions

D.S. conceived the idea and supervised the project. Z.Z. synthesized the Te nanoflakes under the supervision of L.L. and C.G.Z. D.L.L. performed the optical and electrical measurements with the help from S.Y.W., Y.S.Z., M.Y.Q., Y.C.C., J.L. and S.L.C. under the supervision of A.L.P. and D.S.; J.S.Q., C.H. and W.J. performed the numerical calculation; D.L.L. and D.S. wrote the manuscript with input and feedback from all of the authors.

Acknowledgements

This project was supported by the National Natural Science Foundation of China (Grant Nos. 62325401, 62227822 and 12034001) and the National Key Research and Development Program of China (Grant Nos. 2020YFA030880, 2021YFA1400100 and 2022YFA1204300), the authors would also like to acknowledge the National Natural Science Foundation of China (Grant Nos. 52221001 and 62090035), and the Open Fund of State Key Laboratory of Infrared Physics (Grant No. SITP-NLIST-ZD-2023-02).

Conflicts of Interest

The authors declare no conflicts of interest.

Data Availability Statement

The data that support the findings of this study are available from the corresponding author upon reasonable request.

References

1. I. Bente, S. Taheriniya, F. Lenzini, et al., "The Potential of Multidimensional Photonic Computing," *Nature Reviews Physics* 7 (2025): 439–450, https://doi.org/10.1038/s42254-025-00843-3.

2. G. T. Reed, G. Mashanovich, F. Y. Gardes, and D. J. Thomson, "Silicon Optical Modulators," *Nature Photonics* 4 (2010): 518–526, https://doi.org/10.1038/nphoton.2010.179.

3. Y. Meng, J. G. Feng, S. M. Han, et al., "Photonic Van Der Waals Integration from 2D Materials to 3D Nanomembranes," *Nature Review Materials* 8 (2023): 498–517.

4. Z. Shan, X. Hu, X. Wang, et al., "Phonon-Assisted Electro-Optical Switches and Logic Gates Based on Semiconductor Nanostructures," *Advanced Materials* 31 (2019): 1901263, https://doi.org/10.1002/adma.201901263.

5. J. Shang, X. Shen, C. Cong, et al., "Observation of Excitonic Fine Structure in a 2D Transition-Metal Dichalcogenide Semiconductor," *ACS Nano* 9 (2015): 647–655, https://doi.org/10.1021/nn5059908.

6. D. H. Lien, S. Z. Uddin, M. Yeh, et al., "Electrical Suppression of All Nonradiative Recombination Pathways in Monolayer Semiconductors," *Science* 364 (2019): 468–471, https://doi.org/10.1126/science.aaw8053.

7. H. T. Yi, S. Rangan, B. X. Tang, et al., "Electric-Field Effect on Photoluminescence of Lead-Halide Perovskites," *Materials Today* 28 (2019): 31–39.

8. D. Unuchek, A. Ciarrocchi, A. Avsar, K. Watanabe, T. Taniguchi, and A. Kis, "Room-Temperature Electrical Control of Exciton Flux in a van der Waals Heterostructure," *Nature* 560 (2018): 340–344, https://doi.org/10.1038/s41586-018-0357-y.

9. D. Unuchek, A. Ciarrocchi, A. Avsar, et al., "Valley-polarized Exciton Currents in a van der Waals Heterostructure," *Nature Nanotechnology* 14 (2019): 1104–1109, https://doi.org/10.1038/s41565-019-0559-y.

10. A. J. Moilanen, M. Cavigelli, T. Taniguchi, K. Watanabe, and L. Novotny, "Electrical Control of Photoluminescence in 2D Semiconductors Coupled to Plasmonic Lattices," *ACS Nano* 19 (2025): 4731–4738.

11. G. Z. Liang, X. C. Yu, X. N. Hu, B. Qiang, C. W. Wang, and Q. J. Wang, "Mid-Infrared Photonics and Optoelectronics in 2D Materials," *Materials Today* 51 (2021): 294–316.

12. Y. R. Fang, Y. Q. Ge, C. Wang, and H. Zhang, "Mid-Infrared Photonics Using 2D Materials: Status and Challenges," *Laser & Photonics Reviews* 14 (2020): 1900098.

13. R. Soref, "Mid-Infrared Photonics in Silicon and Germanium," *Nature Photonics* 4 (2010): 495–497, https://doi.org/10.1038/nphoton.2010.171.

14. C. Chen, X. Lu, B. Deng, et al., "Widely Tunable Mid-infrared Light Emission in Thin-Film Black Phosphorus," *Science Advances* 6 (2020): aay6134, https://doi.org/10.1126/sciadv.aay6134.

15. S. Wang, N. Higashitarumizu, B. Sari, M. C. Scott, and A. Javey, "Quantitative Mid-Infrared Photoluminescence Characterization of Black Phosphorus–Arsenic Alloys," *ACS Nano* 18 (2024): 5907–5914.

16. J. C. Liang, Y. Hu, K. Q. Zhang, et al., "2D Layered Black Arsenic-Phosphorus Materials: Synthesis, Properties, and Device Applications," *Nano Research* 15 (2022): 3737–3752, https://doi.org/10.1007/s12274-021-3974-y.

17. C. Benoit Àla Guillaume and J. M. Debever, "Emission Spontanee Et Stimulee Du Tellure Par Bombardement Electronique," *Solid State Communications* 3 (1965): 19–20, https://doi.org/10.1016/0038-1098(65)90161-4.

18. A. S. Pine, N. Menyuk, and G. Dresselhaus, "Laser Emission Study of the Pressure Dependence of the Energy Gap in Tellurium," *Solid State Communications* 31 (1979): 187–191, https://doi.org/10.1016/0038-1098(79)90432-0.

19. D. Choi and K. S. Jeong, "Midwavelength Infrared Photoluminescence and Lasing of Tellurium Elemental Solid and Microcrystals," *The Journal of Physical Chemistry Letters* 10 (2019): 4303–4309, https://doi.org/10.1021/acs.jpclett.9b01523.

20. S. Wang, N. Higashitarumizu, M. Jamal, et al., "Mid-Infrared Photoluminescence from Tellurium Thin Films," *Nano Letters* 25 (2025): 9311–9317, https://doi.org/10.1021/acs.nanolett.5c01622.

21. M. Hirayama, R. Okugawa, S. Ishibashi, S. Murakami, and T. Miyake, "Weyl Node and Spin Texture in Trigonal Tellurium and Selenium," *Physical Review Letters* 114 (2015): 206401, https://doi.org/10.1103/PhysRevLett.114.206401.

22. N. M. Gabor, J. C. Song, Q. Ma, et al., "Hot Carrier–Assisted Intrinsic Photoresponse in Graphene," *Science* 334 (2011): 648–652, https://doi.org/10.1126/science.1211384.

23. Y. Zhang, T. T. Tang, C. Girit, et al., "Direct Observation of a Widely Tunable Bandgap in Bilayer Graphene," *Nature* 459 (2009): 820–823, https://doi.org/10.1038/nature08105.

24. D. G. Purdie, N. M. Pugno, T. Taniguchi, K. Watanabe, A. C. Ferrari, and A. Lombardo, "Cleaning Interfaces in Layered Materials Heterostructures," *Nature Communications* 9 (2018): 5387, https://doi.org/10.1038/s41467-018-07558-3.

25. Y. X. Wang, G. Qiu, R. X. Wang, et al., "Field-Effect Transistors Made from Solution-Grown Two-Dimensional Tellurene," *Nature Electronics* 1 (2018): 228–236.

26. G. Jnawali, Y. Xiang, S. M. Linser, et al., "Ultrafast Photoinduced Band Splitting and Carrier Dynamics in Chiral Tellurium Nanosheets," *Nature Communications* 11 (2020): 3991, https://doi.org/10.1038/s41467-020-17766-5.

27. Y. Y. Pan, S. Y. Gao, L. Yang, and J. Lu, "Dependence of Excited-state Properties of Tellurium on Dimensionality: From Bulk to Two Dimensions to One Dimensions," *Physical Review B* 98 (2018): 085135.

28. D. Q. Yang, L. Q. Zhu, J. L. Wang, et al., "Band Structure and Lattice Vibration of Elemental Tellurium Investigated by Temperature-Dependent Mid-and-Far Infrared Transmission and Raman Spectroscopy," *Physica Status Solidi B-Basic Solid State Physics* 259 (2022): 2100625.

29. P. K. Li, "Mid-Infrared Photoconductivity Spectra of Single Tellurium Nanowires," *Journal of Applied Physics* 128 (2020): 063105.

30. A. V. Dmitriev and M. Mocker, "Recombination and Ionization in Narrow-Gap Semiconductors," *Physics Reports-Review Section of Physics Letters* 257 (1995): 85–131.

31. A. Laturia, M. L. Van de Put, and W. G. Vandenberghe, "Dielectric Properties of Hexagonal Boron Nitride and Transition Metal Dichalcogenides: From Monolayer to Bulk " *npj 2D Materials and Applications* 2 (2018): 6.

32. W. P. Dumke, "Spontaneous Radiative Recombination in Semiconductors," *Physical Review* 105 (1957): 139, https://doi.org/10.1103/PhysRev.105.139.

33. L. Li, Y. Yu, G. J. Ye, et al., "Black Phosphorus Field-Effect Transistors," *Nature Nanotechnology* 9 (2014): 372–377.

34. S. L. Chuang, *Physics of Photonic Devices* (Wiley, 2012).

35. Y. Liu, Z. Qiu, A. Carvalho, et al., "Gate-Tunable Giant Stark Effect in Few-Layer Black Phosphorus," *Nano Letters* 17 (2017): 1970–1977, https://doi.org/10.1021/acs.nanolett.6b05381.

36. Z. Sun, K. Xu, C. Liu, et al., "Photoluminescence Switching Effect in a Two-Dimensional Atomic Crystal," *ACS Nano* 15 (2021): 19439–19445, https://doi.org/10.1021/acsnano.1c06016.

37. X. Chen, X. Lu, B. Deng, et al., "Widely Tunable Black Phosphorus Mid-Infrared Photodetector," *Nature Communications* 8 (2017): 1672.

38. C. Wang, X. Zhou, J. Qiao, et al., "Charge-Governed Phase Manipulation of Few-Layer Tellurium," *Nanoscale* 10 (2018): 22263–22269, https://doi.org/10.1039/C8NR07501H.

39. S. C. Liebscher, M. K. Hagen, J. Hader, J. V. Moloney, and S. W. Koch, "Microscopic Theory for the Incoherent Resonant and Coherent Off-Resonant Optical Response of Tellurium," *Physical Review B* 104 (2021): 165201.

40. M. Amani, D. H. Lien, D. Kiriya, et al., "Near-Unity Photoluminescence Quantum Yield in MoS 2," *Science* 350 (2015): 1065–1068, https://doi.org/10.1126/science.aad2114.

41. K. V. Sreekanth, P. Mahalakshmi, S. Han, M. S. M. Rajan, P. K. Choudhury, and R. Singh, "Brewster Mode-Enhanced Sensing with Hyperbolic Metamaterial," *Advanced Optical Materials* 7 (2019): 1900680.

42. Y. Liu, Q. Q. Zhong, D. L. Liang, et al., "Photoluminescence Enhancement of InSe by Coupling with Circular Bragg Grating," *Laser & Photonics Reviews* 17 (2023): 2300234.

43. Y. S. Zhang, S. W. Wang, S. L. Chen, et al., "Wavelength-Tunable Mid-Infrared Lasing from Black Phosphorus Nanosheets," *Advanced Materials* 32 (2020): 1808319.

44. Y. Ye, Z. J. Wong, X. F. Lu, et al., "Monolayer Excitonic Laser," *Nature Photonics* 9 (2015): 733–737, https://doi.org/10.1038/nphoton.2015.197.

45. L. Chang, S. Liu, and J. E. Bowers, "Integrated Optical Frequency Comb Technologies," *Nature Photonics* 16 (2022): 95–108, https://doi.org/10.1038/s41566-021-00945-1.

46. M. Gupta, N. Navaratna, P. Szriftgiser, G. Ducournau, and R. Singh, “327 Gbps THz Silicon Photonic Interconnect with Sub-λ Bends,” *Applied Physics Letters* 123 (2023): 171102.

47. R. Jia, Y. J. Tan, N. Navaratna, A. Kumar, and R. Singh, “Photonic Supercoupling in Silicon Topological Waveguides,” *Advanced Materials* 37 (2024): 2415083.

48. M. Amani, C. Tan, G. Zhang, et al., “Solution-Synthesized High-Mobility Tellurium Nanoflakes for Short-Wave Infrared Photodetectors,” *ACS Nano* 12 (2018): 7253–7263, https://doi.org/10.1021/acsnano.8b03424.

49. Z. L. Hu, Q. Fu, J. P. Lu, et al., “Van der Waals Integrated Single-Junction Light-Emitting Diodes Exceeding 10% Quantum Efficiency at Room Temperature,” *Science Advances* 10 (2024): eadp8045.

50. H. Kim, S. Z. Uddin, D. H. Lien, et al., “Actively Variable-Spectrum Optoelectronics with Black Phosphorus,” *Nature* 596 (2021): 232–237, https://doi.org/10.1038/s41586-021-03701-1.

51. P. E. Blochl, “Projector Augmented-Wave Method,” *Physical Review B* 50 (1994): 17953, https://doi.org/10.1103/PhysRevB.50.17953.

52. G. Kresse and D. Joubert, “From Ultrasoft Pseudopotentials to the Projector Augmented-Wave Method,” *Physical Review B* 59 (1999): 1758, https://doi.org/10.1103/PhysRevB.59.1758.

53. J. Klimes, D. R. Bowler, and A. Michaelides, “Chemical Accuracy for the van der Waals Density Functional,” *Journal of Physics: Condensed Matter* 22 (2010): 022201, https://doi.org/10.1088/0953-8984/22/2/022201.

Supporting Information

Additional supporting information can be found online in the Supporting Information section.

Supporting Information File 1: adma71861-sup-0001-SuppMat.docx